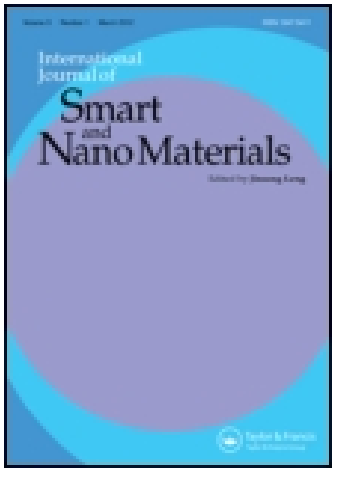

International Journal of Smart and Nano Materials

Publication details, including instructions for authors and subscription information:
http://www.tandfonline.com/loi/tsnm20

Magnetic actuation and transition shapes of a bistable spherical cap

E.G. Loukaides[a], S.K. Smoukov[b] & K.A. Seffen[a]

[a] Department of Engineering, University of Cambridge, Trumpington Road, Cambridge CB2 1PZ, UK

[b] Department of Materials Science and Metallurgy, University of Cambridge, 27 Charles Babbage Road, Cambridge CB3 0FS, UK

Published online: 22 Jan 2015.

To cite this article: E.G. Loukaides, S.K. Smoukov & K.A. Seffen (2014) Magnetic actuation and transition shapes of a bistable spherical cap, International Journal of Smart and Nano Materials, 5:4, 270-282, DOI: 10.1080/19475411.2014.997322

To link to this article: http://dx.doi.org/10.1080/19475411.2014.997322

International Journal of Smart and Nano Materials, 2014
Vol. 5, No. 4, 270–282, http://dx.doi.org/10.1080/19475411.2014.997322

Taylor & Francis
Taylor & Francis Group

Magnetic actuation and transition shapes of a bistable spherical cap

E.G. Loukaides[a]*, S.K. Smoukov[b] and K.A. Seffen[a]

[a]*Department of Engineering, University of Cambridge, Trumpington Road, Cambridge CB2 1PZ, UK;* [b]*Department of Materials Science and Metallurgy, University of Cambridge, 27 Charles Babbage Road, Cambridge CB3 0FS, UK*

(*Received 9 September 2014; final version received 7 December 2014*)

Multistable shells have been proposed for a variety of applications; however, their actuation is almost exclusively addressed through embedded piezoelectric patches. Additional actuation techniques are needed for applications requiring high strains or where remote actuation is desirable. Part of the reason for the lack of research in this area is the absence of appropriate models describing the detailed deformation and energetics of such shells. This work presents a bistable spherical cap made of iron carbonyl-infused polydimethylsiloxane. The magnetizable structure can be actuated remotely through permanent magnets while the transition is recorded with a high-speed camera. Moreover, the experiment is reproduced in a finite element (FE) dynamic model for comparison with the physical observations. High-speed footage of the physical cap inversion together with the FE modeling gives valuable insight on preferable intermediate geometries. Both methods return similar values for the magnetic field strength required for the snap-through. High-strain multistable spherical cap transformation is demonstrated, based on informed material selection. We discover that non-axisymmetric transition shapes are preferred in intermediate geometries by bistable spherical caps. We develop the methods for design and analysis of such actuators, including the feasibility of remote actuation methods for multistable shells.

Keywords: multistable; composites; magnetism; actuation

1. Introduction

Multistable shells are thin-walled structures capable of resting in more than one stable shape. As potential actuator elements, only the transition between states needs to be "powered" continuously and not their rest configurations; thus, there are positive implications for saving energy during operation. Description of actuation methods for them, however, is limited and relevant work is scarce. This is contrary to the actuation of generic, monostable shells, which encompasses an extensive and challenging field. A growing number of "smart materials" can be used for such purposes, and choosing the right one depends on the specific requirements of the application. A review by Huber et al. [1] provides a comprehensive guide, taking into account various performance metrics for simplified actuator design. Beyond choosing an actuator type though, additional decisions have to be made as to the location and number of actuator devices.

*Corresponding author. Email: el249@cam.ac.uk

One such smart material is piezoelectric ceramic, which is formed as a thin strip. They are either attached to the shell surface or, as in the case of the composite laminate shells, embedded within the fiber-reinforced layers. Many studies describe small deformations and quick responses, and, in this regard, piezoelectric actuators are highly advantageous. On the other hand, piezoelectric ceramics have a limited capacity for strain and, consequently, may not be suited for multistable shells, where relatively large strains may occur during large changes in displacements. Composite shells turn out to be ideal candidates for multistable shells because the underlying capability can be tuned by varying the material composition and initial shape: bistable orthotropic shells with cylindrical conformations, for example, are well established by Guest and Pellegrino [2]. The most successful alternative to embedded piezoelectric strips has been macro-fiber composites (MFCs), where larger fibers of piezoelectric rod wrapped in a tough epoxy mingle with smaller inherent structural fibers. Schultz et al. [3] first described MFCs as actuators through experimental and finite element analysis (FEA) demonstrations, and they establish that sufficient internal bending moments can be generated by MFCs to force the transition in cylindrical bistable shells. Extending this work, Portela et al. [4] evaluated its feasibility as a switch between stable states for asymmetrical laminates, and this analysis is matched with corresponding FEA, with moisture effects included; the authors note, however, that the low force capability of MFCs limits the potential size and stiffness of bistable shells. Similar proof-of-concept studies were subsequently performed by other authors [5,6], again using MFCs as the actuating elements.

The simplest bistable isotropic shell is a shallow spherical cap, which can be inverted by turning it inside out: this behavior is well known and has been investigated in depth [7–9]. Caps made of bimetallic material, which is directly isotropic, can respond to a rise in ambient temperature by deforming against the initial curvature. If the deformation is large enough, the shell can "snap-through" and invert, and this principle is exploited in many thermostatic valves – in virtually every domestic kettle [10]. In this sense, thermal loading behaves as the actuating force, but the bistability itself is primarily governed by the initial geometry of the cap, specifically by the thickness and by the ratio of its apex height above the outer rim to its curvature; the cap material governs how stiff the shell is in either of its rest shapes, and the equivalent actuation strain or thermal gradients determine the effectiveness and power requirements for martialing the transition. An alternative actuation mechanism using bistable spherical dimples was presented by Holmes and Crosby [11], where thin, translucent polydimethylsiloxane (PDMS) microlenses are mechanochemically actuated. Here, we advocate the use of a magnetic field for scalable actuation; a force field can control a multistable shell in the nano-scale, but can potentially also do so in the macro-scale. However, additional analysis is required to establish the influence of scale over the competing phenomena, that is, inertia, magnetic forces, elastic forces, and damping. This is complicated further by the high degree of nonlinearity inherent in each facet of behavior, for example, geometrical non-linearity for the shell and spatial non-linearity for the magnetic field.

Analytical models help design multistable shells. The uniform curvature (UC) assumption [12–14] is successful in explaining the behavior around the initial and final configurations of the bistable shell; however, a UC model cannot be used to obtain intermediate geometries accurately because these shapes are typically non-uniform. In precise engineering applications, the shape of the structure at any point in its operation might be a critical parameter, for example, intermediate geometries are particularly important in the design of bistable energy harvesters – a characteristically dynamical application [15]. Moreover, studying the behavior of the structure during actuation can

extend our understanding of this category of shells and promote energetically optimal actuation paths. And most recently, a linearly varying curvature (LVC) assumption was employed by Vidoli [16], to describe transition shapes.

In this study, we construct and remotely actuate a bistable spherical cap by a magnetic field. We analyze the performance using computational software to establish the energetics of the path of various transitions steps adopted between the initial and final configurations. The cap inverts during actuation by turning inside out, which is not unusual given what is known about bistable caps. However, the transition between states is rarely symmetrical, if at all. Instead, when part of the cap begins to displace more than the rest, the asymmetry quickly amplifies, which leads to a dramatically asymmetrical transition mode. The transitional shapes have varying curvature and the UC assumption cannot be used to describe them, so we resort instead to a finite element model of the process, which couples the interactions of the complex asymmetric shapes with the magnetic field, and provides an accurate prediction of the actuation process. We also provide an analytical approximation of the fields around a cylindrical permanent magnet, which have not been available before, and which would facilitate the design of such actuators. Our focus, however, is on capturing the structural features of the transition. Potential applications include all the above, but we also envision that remote magnetic actuation can be a powerful tool for various switches and micro-mechanical devices.

In Section 2, we describe the experimental procedures: the manufacture of the cap, and then the actuation process in terms of how the magnetic field is applied. In Section 3, the details of the FEA are introduced with particular emphasis on modeling the magnetic field: loading cases are considered in which the cap undergoes both symmetrical and asymmetrical inversion during actuation. We interrogate the changes in shape and strain energy stored in the cap.

2. Experimental method

2.1. Shell design and manufacturing

The shell is constructed using a commonplace polymer, cured together with iron particles, thus creating a magnetic rubber composite. The geometrical specifications are as follows: the radius of curvature of the shell is 22 mm for a cap of base radius equal to 18 mm. Various thicknesses are created and tested, in the range of 1–3 mm, matching the gap distances of the moulds. The data presented here are for a shell with thickness of 1.5 mm. Male and female moulds are constructed through 3D printing technology – specifically, the commercially available MakerBot Replicator^{TM} is used [17]. The moulds are sanded and treated with an antistick spray, which helps the removal of the samples after curing.

The material chosen for the shells has an array of advantages. PDMS is commercially available and relatively cheap. From an engineering perspective, it is desirable in this case for its high capacity for deformation (multiple cycles of 100% strain) [18], its formability, its easy curing, and its ability to allow various inclusions – here, iron trimmings are used. For the elastomer, we choose the commercially available Sylgard 184 Silicone Elastomer, while the iron is added to the PDMS at a proportion of 50% by weight and mixed well. The carbonyl iron was obtained from Sigma-Aldrich (product numbers: CAS #7439-89-6, Sigma #44890). The nominal grain size is given as 6–9 μm but many are in the 2–5 μm range.

After pouring the mixture in a mould, the samples are cured for 45 min at 100°, and we give the relevant mechanical properties in Table 1. Once cured and removed from their moulds, the shell caps can be deformed elastically and easily by hand; for each thickness, it is possible to turn the shell "inside-out" completely, so that it has a second, inverted configuration, which is stable without further support. The original, stress-free shapes can be recovered by simply reverting the shape, and this process can be performed many times without the material failing.

2.2. *Experimental setup and observations*

We use a standard mechanical lathe for precisely fixing the elements of our experiment. First, the spherical cap is secured to a thin cylindrical rod by a pin through its center before mounting and securing the rod in the fixed chuck of the lathe. A magnetic field is created by using commercially available high-strength Neodymium N42 cylindrical magnets, with radii of 25 mm and a height of 3 mm. The axis connecting the magnetic poles coincides with their geometrical axis of symmetry. Four of these are mounted in sequence as a stack to increase the flux density, equivalent to a single magnet of the same radius and 12 mm in height. The magnets are then connected, with a pole pointing to the cap, to the movable end of the lathe whose axial position is precisely controlled by a manually operated, threaded screw pitch. Moving the magnets closer to the cap simulates increasing field strength and, hence, larger actuation force in a highly controllable manner. The speed of movement is approximately constant and less than 1 mm/s, bringing the magnet into close proximity of the cap until it inverts in a "snap-through" fashion: this process is filmed at 3000 frames per second, with snap-shots displayed in Figure 1, along with a detailed diagram of the setup. The rate of magnet movement is much slower than the dynamic inversion itself, so we can assume the setup to be stationary for the duration of the shell transition, which takes place in about 0.1 s.

The high-speed camera is a Phantom v12.0 [20]: for a few tenths of a second capturing the full transition, we are afforded a few hundred image frames. At such high shutter speeds, high luminance is required and provided by off-the-shelf floodlights. The brightness of the images is digitally augmented afterwards to enhance the contrast between the shell and the background – the software provided with the camera includes this feature.

In every tested case, the inversion is not radially symmetrical; typically, one side of the cap is first pulled closer to the magnets, which can be clearly seen in Figure 1. On the opposite edge of the shell, the rim moves backwards, increasing the relative displacement between the cap and the magnets there, and a temporary S-shape in the central diametral line is observed. As the approach becomes closer, the tendency is for the S-shape to remain; the strength of the magnetic field is, however, large enough to overwhelm the shape, and the shell is pulled through to a fully inverted geometry. Since the external body force is not immediately removed, the edges continue deforming toward the magnets beyond the natural, load-free inverted configuration. This extra deformation forces the inverted cap into a cylindrical shape, which makes contact with the magnets on opposing sides of the rim where the rim is the closest; shortly afterwards, virtually all of the rim becomes in contact, as shown in Figure 2. When the magnet is pulled away, the shell remains inverted with an approximately spherical geometry, but with a narrow edge lip corresponding to opposite-sense curvatures on the periphery.

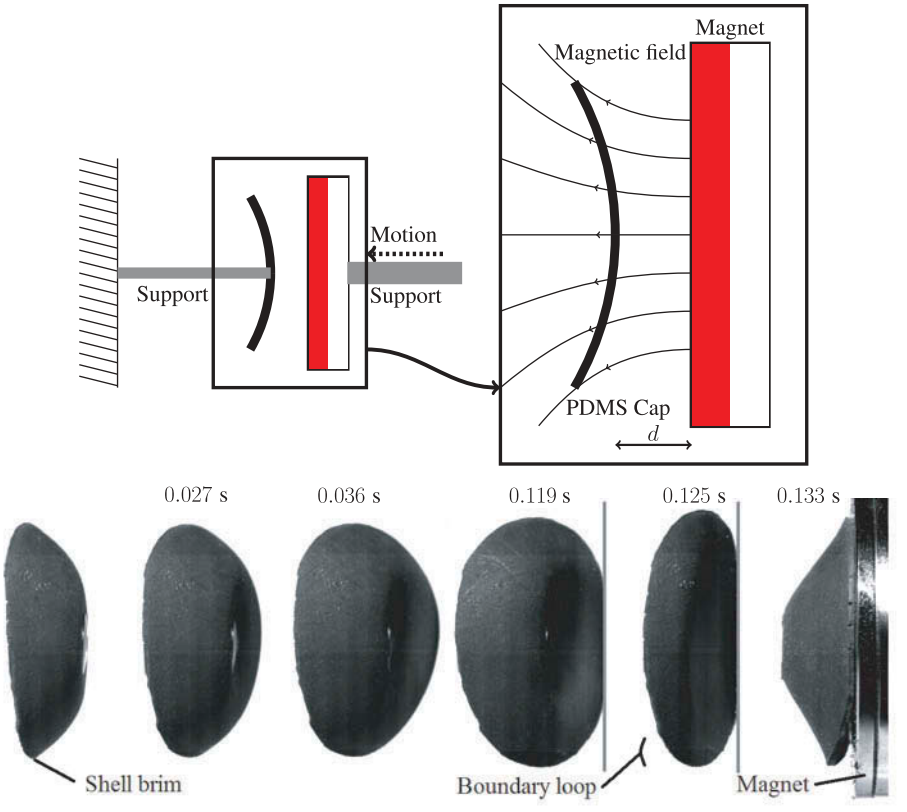

Figure 1. Diagram of the experimental setup for remotely actuating a PDMS spherical cap with a permanent magnet (top). The cap is stationary while the magnet is moved via a support toward the cap until a snap-through is observed. A high-speed camera captured the transition of the shell (bottom) – an event that approximately lasts a tenth of a second (0.14 s for the frames shown above). One noteworthy aspect of the transition is the non-axisymmetrical geometry that develops during the snap-through. Most noticeably from this angle, at $t = 0.119\,\mathrm{s}$, the furthest point from the camera fully reverses before the closest point to the camera begins to develop a new curvature. This is a consequence of the high circumferential stiffness at the brim of the shell. The "boundary loop" is opposing stretching, and bending action is favored in the shell's global response.

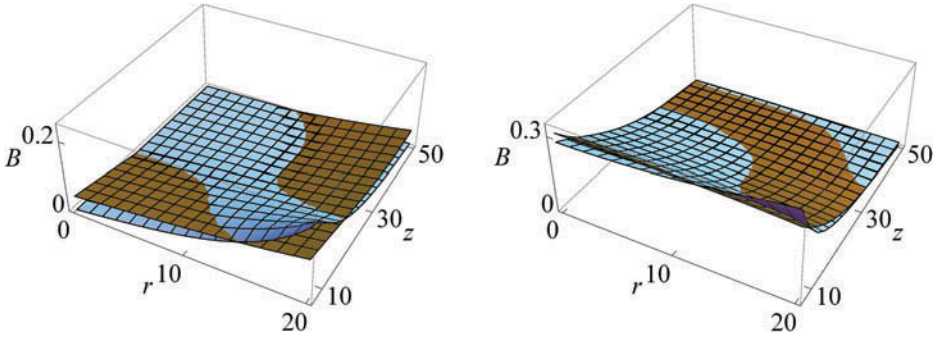

Figure 2. The radial (left) and axial (right) components of the magnetic field of a permanent cylindrical magnet. The blue surface represents a numerical estimation of the field and the brown surface shows a polynomial best-fit obtained in Mathematica and used in Abaqus.

3. Finite element model

In addition to the photographic data, a finite element model is constructed for comparison and quantitative analysis. Abaqus/CAE [21] is used to design a model matching the physical shell described above. The material elastic properties are defined to match those in Table 1, where we state values for the Young's modulus, the shear modulus and the Poisson's ratio. We model the material as linear elastic, although the Mooney–Rivlin model would be appropriate for reproducing greater detail. The density of the simulated shell is the weighted average of the densities of PDMS and iron particles as given in Table 2, thus providing the inertia properties of the model. No damping is defined explicitly in the model, but dissipation is a feature of the numerical solver.

The initial mesh was generated by a swept shell configuration available in the Abaqus graphical user interface, of dimensions equal to the physical shell: the final mesh has 1571 linear quadrilateral elements of type S4R. We fix a circular area in the center of the part to simulate the pin constraint, while the magnetic field is modeled as a quasi-static body force applied to the cap; this force has a spatially varying amplitude, which is explained further in the following section. A dynamic implicit step is specified for the loading phase, and non-linear changes in geometry are permitted given the expectation of relatively large displacements. In its simplest form, the equation solved by Abaqus can be written as:

$$\vec{f} = \vec{F} - \rho\vec{\ddot{u}} \tag{1}$$

where $\vec{f}$ is the total body force at a point, given by an externally prescribed body force, $\vec{F}$, and a d'Alembert force [22] (ρ is the density and $\vec{\ddot{u}}$ the acceleration). As mentioned above, no damping is defined in the simulation, but the solver provides numerical dissipation. Specifically, the time integration is performed via the backward Euler operator, and the resulting numerical damping depends on the choice of time step. This in turn is chosen by

Table 1. Approximate mechanical properties for PDMS; E, the Young's modulus and G, the shear modulus, are taken from the study by Lötters et al. [19], ν, the Poisson's ratio is given the commonly accepted value for rubbers.

E (kPa)	G (kPa)	ν
750	250	0.5

Table 2. Magnetic and material properties needed to estimate the magnetic force between a Neodymium, N42 grade permanent magnet, and an iron/carbonyl-infused PDMS structure.

Property	Reference	Value
PDMS specific gravity	Dow Corning [26]	1.03
$\delta\chi$	Gorodkin et al. [27],	0.20
Iron specific gravity		7.87
Neodymium magnetization/volume	K&J Magnetics, Inc. [28]	$1.03 \times 10^6 \mathrm{A/m}$
μ_0	Lide [29],	$4\pi \times 10^{-7} \mathrm{N/A^2}$

monitoring the dissipation energy in our model, and by having established a realistic duration for the oscillations experimentally.

The force is applied instantaneously on the structure while the duration of the Abaqus Step (model time range) is 0.1 s, which sufficiently captures all of the deformation, beyond the snap-through. The maximum time increment of the solver is 0.0004 s so that the data points are finely resolved and rapidly changing features are accurately described, but also to control numerical damping as mentioned earlier.

3.1. *Magnetic field and force*

The magnetic field of a permanent magnet is not always straightforward to calculate and that may be one of the reasons it is less widely used than the availability of permanent magnets may suggest. It depends on the exact geometry of the magnet itself, on the magnetic material, as well as the surrounding medium. The calculation involves multiple integrals over a complex integrand [23], which we derive for the magnet in our experiment. Here, we use a numerical estimation from Blinder [24], for a cylindrical permanent magnet which involves a triple integral that is solved numerically in cylindrical coordinates. Specifically, the axial and radial components of the magnetic field are, B_z and B_r, respectively, and are given by:

$$B_z = -\frac{\mu_0}{4\pi} M \int_0^{2\pi} \int_0^a \left(\frac{R(L/2 - z)}{\left(R^2 + (L/2 - z)^2 + r^2 - 2Rr\,\cos\Phi\right)^{3/2}} + \frac{R(L/2 + z)}{\left(R^2 + (L/2 + z)^2 + r^2 - 2Rr\,\cos\Phi\right)^{3/2}} \right) \mathrm{d}R\,\mathrm{d}\Phi \tag{2}$$

$$B_r = -\frac{\mu_0}{4\pi} M \int_0^{2\pi} \int_0^a \left(\frac{R(2r - 2R\,\cos\Phi)}{2\left(R^2 + (L/2 - z)^2 + r^2 - 2Rr\,\cos\Phi\right)^{3/2}} + \frac{R(2r - 2Rcos\Phi)}{2\left(R^2 + (L/2 + z)^2 + r^2 - 2Rr\,\cos\Phi\right)^{3/2}} \right) \mathrm{d}R\,\mathrm{d}\Phi. \tag{3}$$

The magnet has axial length L, radius a, and the cylindrical coordinate system for the source is (R, Φ, z) while (r, ϕ, z) is the corresponding coordinate system for the field: μ_0 is the magnetic susceptibility of free space. In order to calculate the magnetic field intensity, we also need the magnetic moment per unit volume for iron carbonyls, M (A/m).

The FindFit function in Mathematica is used to obtain an analytical expression usable in Abaqus: suitable polynomial expressions are chosen for both the radial and axial components of the field and the corresponding coefficients are found through a least-square fit. Specifically, the assumed polynomials take the form:

$$a_0 + a_1 r + a_2 r^2 + a_3 r^3 + a_4 z + a_5 z^2 + a_6 z^3. \tag{4}$$

A comparison between the polynomial, best-fit expression and the original, analytical expression is plotted in Figure 2 and shows a close match (we provide goodness-of-fit metrics in a supplementary table.) Abaqus allows the definition of fields through analytical expressions and, in turn, the analytical expressions are used to define a body force-type load.

The corresponding body force depends on both the magnetic field and the concentration of the carbonyl iron particles, and is formally defined by:

$$\vec{F} = \frac{(\delta\chi)V\vec{B}\cdot\nabla\cdot\vec{B}}{\mu_0} \tag{5}$$

which is taken from the study by Veeramachaneni and Carroll [25], where $\delta\chi$ is the volume magnetic susceptibility difference between the particle and the surrounding medium, V is the magnetizable volume of the particles, B is the magnetic flux density in Tesla (T) and ∇ is the gradient operator in cylindrical coordinates, that is,

$$\nabla = \frac{\partial}{\partial r}\hat{r} + \frac{\partial}{\partial z}\hat{z}. \tag{6}$$

In Abaqus, we express this as the analytical field of a body force; hence the volume is directly taken from the model for each element. As explained above, the magnetic field and consequently its gradient are obtained approximately in closed form. The values of the remaining relevant parameters used in Equation (5) are listed in Table 2. Our model does not take into account the effect of the shell itself on the magnetic field. However, the analytical definition of the field in Abaqus allows the force to be updated in response to the changing geometry in every time-step.

3.2. *Loading cases*

Two separate models are tested. In one, the shell, the boundary condition and the magnetic force are all modeled as perfectly axisymmetric, giving rise to the same deformation mode. In the other, an angular tilt of 5° is applied to the shell at the apex with respect to the x-axis. This slight modification helps explain the non-axisymmetric transition geometries. Even for slight angular eccentricity, the transition shapes differ significantly from axisymmetric geometries. For both these cases, the strategy for the simulations is to initially place the shell at a certain distance from the virtual center of the magnet, d. During a single dynamic step, the body force is continuously applied. We then perform a series of simulations starting with the magnet at 10 mm, 11 mm, 12 mm, 13 mm, 14 mm and 15 mm from the magnet. The snap-through did not occur when the magnet is 14 mm away from the shell for both the axisymmetric and the eccentric cases; the same is observed for 15 mm, so we may reasonably assume that the limiting distance for snap-through is 14 mm.

We mainly focus on two quantitative outcomes extracted from the data of these simulations. First, the total strain energy of the shell is plotted for four separate scenarios in Figures 3 and 4. On the former plot we show the axisymmetric case, while on the latter plot the eccentric case, and within each plot, two tests in which snap-through does occur and does not. For each pair of tests, the strain energy profiles have similar, as well as differing, features, which are now described.

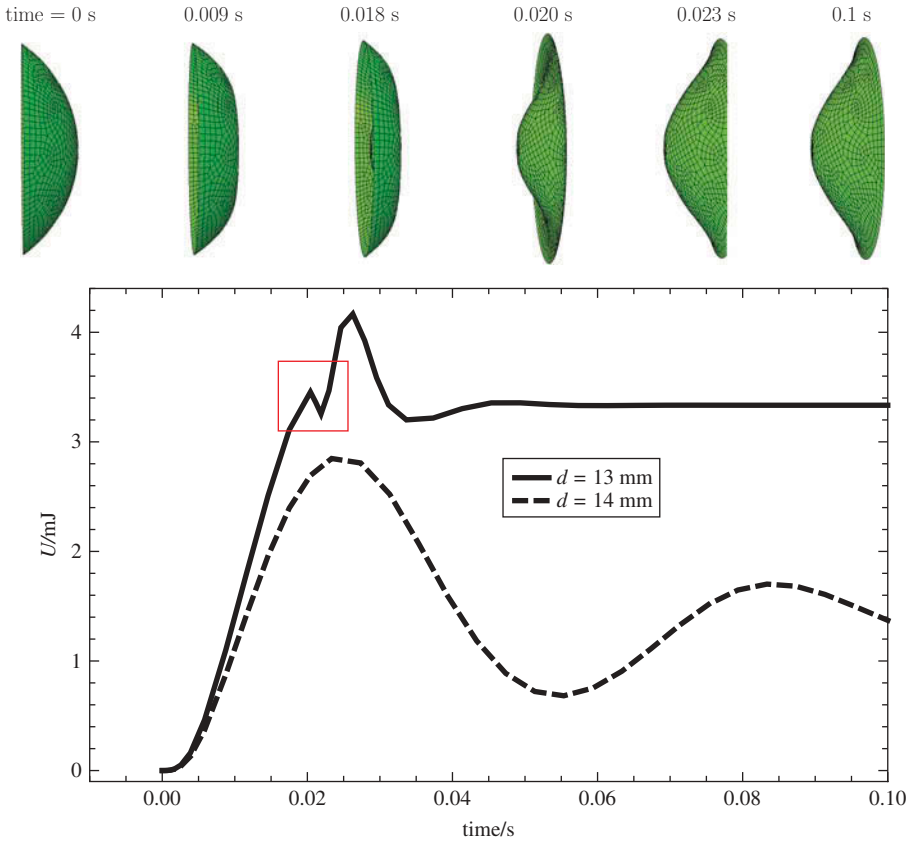

Figure 3. Strain energy plots for FE simulations of a symmetrically supported shell (bottom). A series of simulations were performed at different distances to mark the location of the transition location – shown here to be between 13 and 14 mm. The successful transitions display a snap-through event and an energy minimum marked on the plots with a red square. The FE simulations afford us a closer look at the intermediate geometries (top). For the idealized symmetric case, the transition shapes are axisymmetric, an effect that we were unable to capture in a physical setup. Shown here is the spherical cap, with its center at a distance of 13 mm from the center of the magnet we describe in the text. The magnetic poles are along the z-direction.

When the field is not close enough for snap-through to occur, the strain energy rises first to its largest peak and then reduces, before oscillating about a smaller energy level as time progresses. In both cases, this initial rise corresponds to the shell steadily deforming and moving closer to the magnet. As the displacements increase, the level of (un-)bending increases, which is stored as one component of strain energy; the shell also acquires membranal, or stretching, strain energy, because there are tangential components of loading to the shell surface. But stretching and bending of any surface are fundamentally coupled by Gauss' Theorema Egregium [30], which quantifies this compatibility requirement, so even without tangential body forces, we expect a rise in the stretching component. As the cap begins to invert, the non-linear changes in its geometry permit partial relief of stretching as the change in shell curvature continues to increase, and this is expressed by the first peak and following reduction. The cap moves closer to the magnet and the field strength increases but not to a level which enables, or

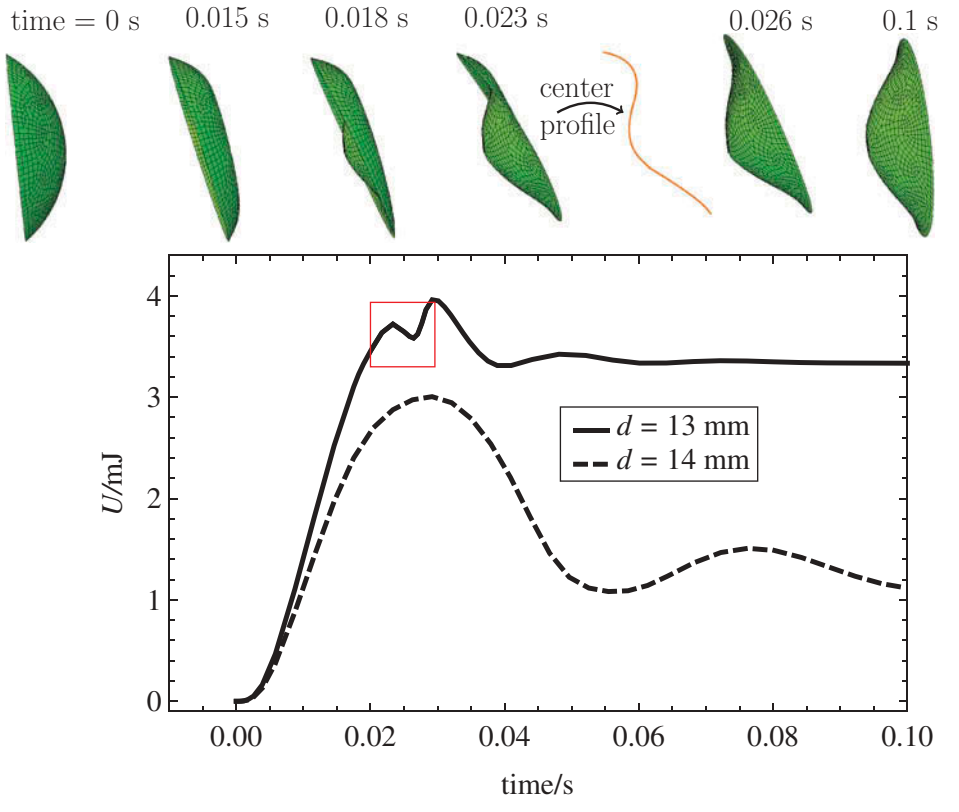

Figure 4. Here, the simulation in Figure 3 is modified. When a slight eccentricity is introduced to the initial tilt of the shell with respect to the direction of the magnetic field, a dramatic change in intermediate geometries is observed. Specifically, the characteristic S-shaped transition shape ($t = 0.023$ s) is preferred by the structure, which agrees with our experimental observations – note that the perspective shown here is at 90° to the perspective of the experimental observation. This shape resembles a surface with linearly varying curvature in one direction across the shell planform, and a uniform curvature in the other direction. A similar geometry is examined by Vidoli [16].

initiates, the snap-through for a full inversion. The shell now retards dynamically, arrests in the sense of reaching a maximum displacement, before springing back, accelerating, and then repeating the process over again. The mean oscillation position corresponds to a quasi-static equilibrium configuration of the cap which would be achieved if the field force were applied incrementally over a much longer time step without inertial effects, which inevitably increases the required computational time frame.

When snap-through occurs in both cases, the strain energy initially rises at a faster rate with time because the field is closer and, hence, the body forces applied to the cap are larger. There are small up-down-up features with a miniature peak and trough highlighted, which correspond to the initiation of both snap-through events. Although the corresponding time periods are very small (<0.005 s), the changes in shape are rapid as evinced by the intermediate geometries in view. This timescale is in rough agreement with the experiment footage, where there are approximately 20 frames between the discernible extreme S-shape geometry and the inverted configuration. The first small peak represents the same onset of stretching relief as before, but

because the body forces are larger, they precipitate full inversion where the cap is now closer to the magnet than before. The larger body forces now stretch the inverted cap with little bending as shown in the inlay, so once again, a process of dynamical retardation and (barely perceptible) oscillation follows (here, as a consequence of numerical damping); the strain energy levels are higher than in the first test because the body forces are larger.

The distorted shapes are clearly very different, and we note that the characteristic S-shaped geometry – also shown in our high-speed photography footage – is observed for the eccentric case. Another difference is that higher strain energy levels are associated with the eccentric case than for the axisymmetrical case almost everywhere. This appears counterintuitive because we would normally expect the strain energy stored in any structure to be a minimum, which ultimately sets the deformation and preferred mode shape when there are multiple load paths. It is important to remember that Figures 3 and 4 only provide a snap-shot of the strain energy stored at a given instant – they are not quasi-static equilibrium paths. Also, the body forces applied to each cap increase with the displacements they induce. For the eccentric case, one side is always pulled closer to the magnet when the other moves away, but the non-linear character of the attractive force always ensures that the net force on the cap is favored by the effects of the near side displacements (a force–displacement plot is also included in supplementary materials.) Furthermore, the plots describe the effectiveness of the actuating force in this regard; if the strain energy level is higher, then the force is able to exert more deformation; this is only possible if the cap is more compliant in terms of its deformation. Thus, the preferred mode is not one which minimizes the strain stored in the cap, rather it is the one which maximizes the effort of – or work done by – the actuating force. That is, the asymmetric shape has a lower stain energy content to overcome.

4. Concluding remarks

PDMS, a material, common in fields such as microfluidics, flexible optics, soft lithography, and soft robotics, is suggested for multistable shells, such that remote actuation is facilitated. Specifically, PDMS infused with iron particles is used for the construction of a bistable, spherical cap. The result is a structure susceptible to magnetic actuation.

For the first time, the dynamic transition of the shell between the original and inverted states under the influence of a magnetic field is captured on a high-speed camera. Footage of the 0.1-s transition is useful in observing intermediate geometries.

Quantitative understanding of the inversion mechanism is made possible by exact finite element modeling of the cap throughout the deformation, which yields the system's strain energy during actuation.

Both the experimental work and the non-idealized FE model show an S-shaped transition shape and not an axisymmetric geometry. This type of configuration cannot be described by some analytical models, such as the UC assumption, but it is likely solvable by the LVC model [16]. Thus, the LVC model is potentially suitable for analytical analysis and design of such and other multistable actuators.

Disclosure statement

No potential conflict of interest was reported by the authors.

Funding

EGL acknowledges financial support by the Alexander S. Onassis Public Benefit Foundation and the Cyprus State Scholarship Foundation. SKS acknowledges funding by the European Research Council (ERC) grant EMATTER [#280078].

Supplemental data

Supplemental data for this article can be accessed here.

References

[1] J. Huber, N. Fleck, and M. Ashby, *The selection of mechanical actuators based on performance indices*, Proc. R. Soc. London Ser. A Math. Phys. Eng. Sci. 453 (1997), pp. 2185–2205. doi:10.1098/rspa.1997.0117

[2] S. Guest and S. Pellegrino, *Analytical models for bistable cylindrical shells*, Proc. R. Soc. A Math. Phys. Eng. Sci. 462 (2006), pp. 839–854. doi:10.1098/rspa.2005.1598

[3] M.R. Schultz, M.W. Hyer, R. Brett Williams, W. Keats Wilkie, and D.J. Inman, *Snap-through of unsymmetric laminates using piezocomposite actuators*, Compos. Sci. Technol. 66 (2006), pp. 2442–2448. doi:10.1016/j.compscitech.2006.01.027

[4] P. Portela, P. Camanho, P. Weaver, and I. Bond, *Analysis of morphing, multi stable structures actuated by piezoelectric patches*, Comput. Struct. 86 (2008), pp. 347–356. doi:10.1016/j.compstruc.2007.01.032

[5] P.F. Giddings, H.A. Kim, A.I. Salo, and C.R. Bowen, *Modelling of piezoelectrically actuated bistable composites*, Mater. Lett. 65 (2011), pp. 1261–1263. doi:10.1016/j.matlet.2011.01.015

[6] M. Gude, W. Hufenbach, and C. Kirvel, *Piezoelectrically driven morphing structures based on bistable unsymmetric laminates*, Compos. Struct. 93 (2011), pp. 377–382. doi:10.1016/j.compstruct.2010.09.004

[7] G. Brodland and H. Cohen, *Deflection and snapping of spherical caps*, Int. J. Solids Struct. 23 (1987), pp. 1341–1356. doi:10.1016/0020-7683(87)90001-1

[8] W. Wittrick, D. Myers, and W. Blunden, *Stability of a bimetallic disk*, Q. J. Mech. Appl. Math. 6 (1953), pp. 15–31. doi:10.1093/qjmam/6.1.15

[9] W. Chien and H. Hu, *On the snapping of a thin spherical cap*, Proc. Ninth Int. Congr. Appl. Mech. 6 (1956), pp. 309–337.

[10] B.D. Aggarwala and E. Saibel, *Thermal stability of bimetallic shallow spherical shells*, Int. J. Non Linear Mech. 5 (1970), pp. 49–62. doi:10.1016/0020-7462(70)90039-9

[11] D. Holmes and A. Crosby, *Snapping surfaces*, Adv. Mater. 19 (2007), pp. 3589–3593. doi:10.1002/adma.200700584

[12] K. Seffen, *Morphing bistable orthotropic elliptical shallow shells*, Proc. R. Soc. A Math. Phys. Eng. Sci. 463 (2007), pp. 67–83. doi:10.1098/rspa.2006.1750

[13] S. Vidoli and C. Maurini, *Tristability of thin orthotropic shells with uniform initial curvature*, Proc. R. Soc. A Math. Phys. Eng. Sci. 464 (2008), pp. 2949–2966. doi:10.1098/rspa.2008.0094

[14] A. Fernandes, C. Maurini, and S. Vidoli, *Multiparameter actuation for shape control of bistable composite plates*, Int. J. Solids Struct. 47 (2010), pp. 1449–1458. doi:10.1016/j.ijsolstr.2010.02.007

[15] D. Betts, H. Kim, C. Bowen, and D. Inman, *Static and dynamic analysis of bistable piezoelectric-composite plates for energy harvesting*, 53rd AIAA/ASME/ASCE/AHS/ASC Structures, Structural Dynamics and Materials Conference 20th AIAA/ASME/AHS Adaptive Structures Conference 14th AIAA, Honolulu, HI, 2012. doi:10.2514/6.2012-1492

[16] S. Vidoli, *Discrete approximations of the Föppl-Von Kármán shell model: From coarse to more refined models*, Int. J. Solids Struct. 50 (2013), pp. 1241–1252. doi:10.1016/j.ijsolstr.2012.12.017

[17] MakerBot Industries, LLC, 2012.

[18] T.K. Kim, J.K. Kim, and O.C. Jeong, *Measurement of nonlinear mechanical properties of PDMS elastomer*, Microelectron. Eng. 88 (2011), pp. 1982–1985. doi:10.1016/j.mee.2010.12.108

[19] J. Lötters, W. Olthuis, P. Veltink, and P. Bergveld, *The mechanical properties of the rubber elastic polymer polydimethylsiloxane for sensor applications*, J. Micromech Microeng. 7 (1997), pp. 145. doi:10.1088/0960-1317/7/3/017
[20] Vision Research Inc., 2013.
[21] Simulia, Dassault Systémes, *Abaqus/CAE User's Manual*, ABAQUS Documentation, Dassault Systèmes, Providence, RI, 2007.
[22] Simulia, Dassault Systémes, *Abaqus Theory Manual*, Version 6.11, ABAQUS Documentation, Dassault Systèmes, Providence, RI, 2011.
[23] M. McCraig and A.G. Clegg, *Permanent Magnets in Theory and Practice*, 2nd ed., John Wiley and Sons, New York, 1987.
[24] S. Blinder, *Magnetic field of a cylindrical bar magnet*, Wolfram Demonstrations Project, 2011.
[25] U.K. Veeramachaneni and R.L. Carroll, *Magnetic particle motion in a gradient field*, Proceedings of the COMSOL Conference, Boston, MA, 2007
[26] Dow Corning, *Sylgard 184 Silicone Elastomer, Product Information*, Corning, 2007. Available at http://www.dowcorning.com/applications/search/products/details.aspx?prod=01064291
[27] S. Gorodkin, R. James, and W. Kordonski, *Magnetic properties of carbonyl iron particles in magnetorheological fluids*, J Phys Conf Ser. 149 (2009), pp. 1–4.
[28] K&J Magnetics, Inc, *Permanent neodymium magnet demagnetization curves*, 2014. Available at http://www.kjmagnetics.com/pdfs/N42_KJM_DemagnetizationCurves.pdf
[29] D.R. Lide, *CRC Handbook of Chemistry and Physics*, CRC Press, Boca Raton, FL, 2004.
[30] K.F. Gauss, *The Project Gutenberg EBook of General Investigations of Curved Surfaces of 1827 and 1825*, 2011.